

Mechanistic Aspects of the Evolution of 3D Cholesterol Crystallites in a Supported Lipid Membrane via a Quartz Crystal Microbalance with Dissipation Monitoring

Gamaliel Junren Ma, Vladimir P. Zhdanov, Soohyun Park, Tun Naw Sut, and Nam-Joon Cho*



Cite This: <https://doi.org/10.1021/acs.langmuir.1c00174>



Read Online

ACCESS |

Metrics & More

Article Recommendations

ABSTRACT: The irreversible formation of cholesterol monohydrate crystals within biological membranes is the leading cause of various diseases, including atherosclerosis. Understanding the process of cholesterol crystallization is fundamentally important and could also lead to the development of improved therapeutic strategies. This has driven several studies investigating the effect of the environmental parameters on the induction of cholesterol crystallite growth and the structure of the cholesterol crystallites, while the kinetics and mechanistic aspects of the crystallite formation process within lipid membranes remain poorly understood. Herein, we fabricated cholesterol crystallites within a supported lipid bilayer (SLB) by adsorbing a cholesterol-rich bicellar mixture onto a glass and silica surface and investigated the real-time kinetics of cholesterol crystallite nucleation and growth using epifluorescence microscopy and quartz crystal microbalance with dissipation (QCM-D) monitoring. Microscopic imaging showed the evolution of the morphology of cholesterol crystallites from nanorod- and plate-shaped habits during the initial stage to mostly large, micron-sized three-dimensional (3D) plate-shaped crystallites in the end, which was likened to Ostwald ripening. QCM-D kinetics revealed unique signal responses during the later stage of the growth process, characterized by simultaneous positive frequency shifts, nonmonotonous energy dissipation shifts, and significant overtone dependence. Based on the optically observed changes in crystallite morphology, we discussed the physical background of these unique QCM-D signal responses and the mechanistic aspects of Ostwald ripening in this system. Together, our findings revealed mechanistic details of the cholesterol crystallite growth kinetics, which may be useful in biointerfacial sensing and bioanalytical applications.



INTRODUCTION

Cholesterol is an essential component of the cell lipid membrane and contributes to membrane structure, permeability, and mechanical properties.^{1–4} Although a high cholesterol content within the membrane can be beneficial, for example, in maintaining the function of human eye lens fiber cells,^{5,6} excessive amounts of cholesterol in other organs can cause the formation of three-dimensional (3D) cholesterol monohydrate crystals that are associated with diseased states such as gallstone formation,^{7,8} atherosclerosis,^{9,10} age-related macular degeneration,¹¹ and demyelinating diseases.¹² This has driven various studies in an effort to understand the biological and physicochemical principles that guide cholesterol crystal formation within the lipid membrane. Toward this objective, model membranes that retain the lipid bilayer structure while simplifying the overall system were developed and have been instrumental in studying complex biological membrane systems.^{13–16}

Within this scope, the supported lipid bilayer (SLB) is a highly useful model membrane system that can be studied using a wide range of surface-sensitive measurement

techniques and also used in bioanalytical and sensing applications.^{17,18} This can be achieved by tracking the change of the cholesterol crystallites within the SLB during their growth and any subsequent processes in a time-resolved manner. Although several methods have been employed for the fabrication of SLBs containing two-dimensional (2D) cholesterol crystalline domains,^{19–21} a few of them have allowed for time-resolved characterization of 3D cholesterol crystallite growth within an SLB. One of them involved a three-phase system of (i) cholesterol in chloroform, (ii) cyclodextrin and cholesterol in water, and (iii) a cholesterol-rich SLB to fabricate 3D cholesterol crystals.^{22,23} While this method allows for visual observation of the crystallite morphology at certain points in time, it is also desirable to characterize the evolution

Received: January 19, 2021

Revised: March 25, 2021

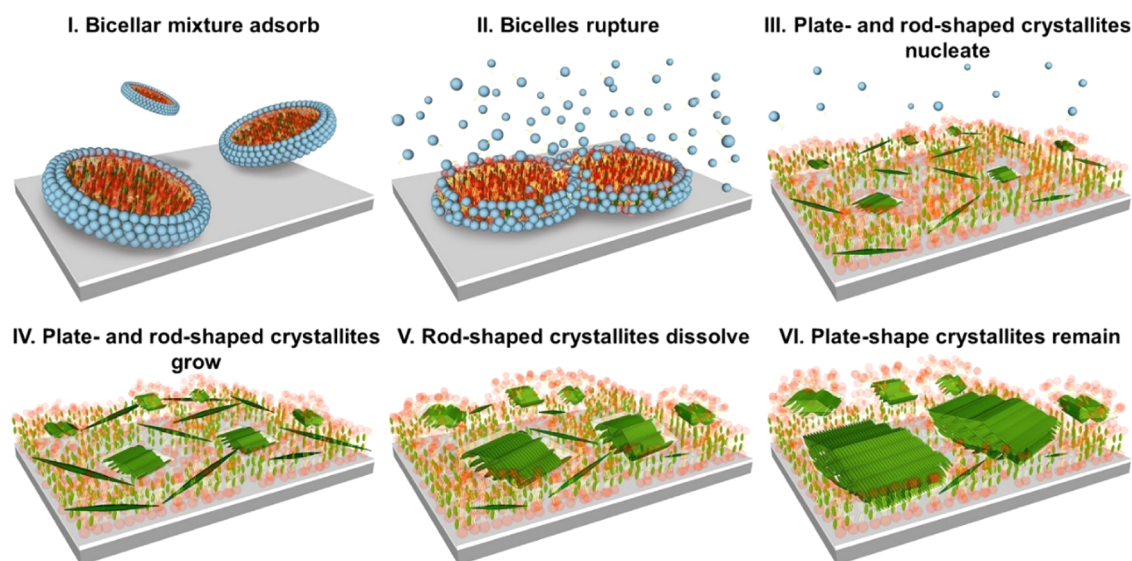


Figure 1. Schematic illustration of cholesterol crystallite nucleation and growth within an SLB from the adsorption of cholesterol-rich bicellar mixture onto a solid surface (disklike conventional bicelles are shown here as a cartoon). Long-chain phospholipids, cholesterol molecules, and short-chain phospholipids are colored red, green, and light blue, respectively. The entire process can be classified into six steps. (I) Cholesterol-rich bicellar mixture adsorbs onto a glass or silica surface. (II) Upon achieving a sufficiently high adsorption uptake, the bicelles rupture and fuse to form a cholesterol-rich SLB. (III) Cholesterol crystallites begin to nucleate within the SLB. (IV) Cholesterol crystallites grow to form rod-shaped and plate-shaped crystal habits. (V) Rod-shaped crystallites begin to dissolve as indicated by their size reduction, while plate-shaped crystallites continue to grow. (VI) Equilibrium is reached, and large plate-shaped crystallites mostly remain.

of cholesterol crystallites in real time using both imaging- and surface-based analytical techniques.

To this end, we recently demonstrated a novel method to fabricate 3D cholesterol crystallites in an SLB through the adsorption of a cholesterol-rich bicellar mixture onto a glass and silica surface.²⁴ Using this approach, it was possible to observe the formation of an SLB and subsequent cholesterol crystallite growth in real time through epifluorescence microscopy and a surface-sensitive measurement technique like a quartz crystal microbalance with dissipation (QCM-D). The real-time monitoring capabilities of this platform were demonstrated by the observation of various transient cholesterol crystal habits within the SLB and also by the observation of the cholesterol crystallites' response to cyclodextrin molecules. Along this line, there remains an outstanding need to improve our fundamental understanding of how cholesterol crystallites nucleate and grow within an SLB during adsorption of the bicellar mixture. While morphological changes can be investigated by epifluorescence microscopy imaging, a detailed analysis of the QCM-D measurement kinetics can yield deeper mechanistic insights into the cholesterol crystallite growth process that cannot be measured through imaging alone. While other surface-sensitive measurement techniques such as the optical-based nanoplasmonic sensors have been employed to study lipid membrane-related biointerfacial events on account of their shorter penetration depth,^{25–28} the acoustic-based QCM-D technique is able to provide additional information on hydrodynamic coupling, which is especially relevant in investigating particulate systems,^{29,30} in this case, cholesterol crystallites.

Herein, we investigated the adsorption behavior of a cholesterol-rich bicellar mixture onto a glass or silica surface including the formation of an SLB and the subsequent growth and evolution of 3D cholesterol crystallites within the membrane in real time. The bicellar mixture was fluorescently labeled to visualize both phospholipid and cholesterol

molecules using epifluorescence microscopy and to track changes in the morphology of cholesterol crystallites during their growth, and the specifics of the observed Ostwald ripening of cholesterol crystallites were further analyzed. The first five QCM-D harmonics were recorded to characterize the corresponding mass and viscoelasticity changes and the underlying physics.

MATERIALS AND METHODS

Reagents. Chloroform-dissolved 1,2-dioleoyl-*sn*-glycero-3-phosphocholine (DOPC), 1,2-dihexanoyl-*sn*-glycero-3-phosphocholine (DHPC), 1,2-dioleoyl-*sn*-glycero-3-phosphoethanolamine-*N*-(lissamine rhodamine B sulfonyl) (ammonium salt) (red, Rh-PE), 23-(dipyrometheneboron difluoride)-24-norcholesterol (green, BODIPY-Chol) lipids, and cholesterol powder were obtained from Avanti Polar Lipids (Alabaster, AL). Rh-PE and BODIPY-Chol have excitation/emission wavelengths of 560/583 and 495/507 nm, respectively. All aqueous lipid sample solutions were prepared in a 10 mM Tris, 150 mM NaCl, pH 7.5 buffer solution prepared with Milli-Q-treated water (resistivity of >18.2 M Ω ·cm at 25 °C).

Sample Preparation. The bicellar mixture was prepared by dissolving cholesterol powder in chloroform in glass vials followed by mixing with DOPC phospholipids to yield a long-chain lipid mixture with 80 mol % cholesterol. For fluorescence microscopy experiments, appropriate amounts of lipids were added such that the resulting lipid mixture contained 0.5 mol % Rh-PE with respect to DOPC amount and 0.5 mol % BODIPY-Chol with respect to the cholesterol amount. The chloroform was then evaporated under a gentle stream of nitrogen gas to form a dry lipid film on the interior walls of the glass vial. The vials were stored overnight in a vacuum desiccator to remove residual traces of chloroform followed by hydration with an aqueous buffer solution containing DHPC phospholipids to yield a lipid suspension of 4 mM short-chain DHPC and 1 mM long-chain lipid mixture (*q*-ratio 0.25). The lipid suspension was then subject to five freeze–thaw–vortex cycles, as previously described.³¹ Each cycle involves freezing by submersion in liquid nitrogen for 1 min, thawing by submersion in a 60 °C water bath for 5 min, then 30 s of vortex mixing. Prior to each experiment, an aliquot of the resulting stock lipid suspension was diluted in the buffer solution to yield a sample of

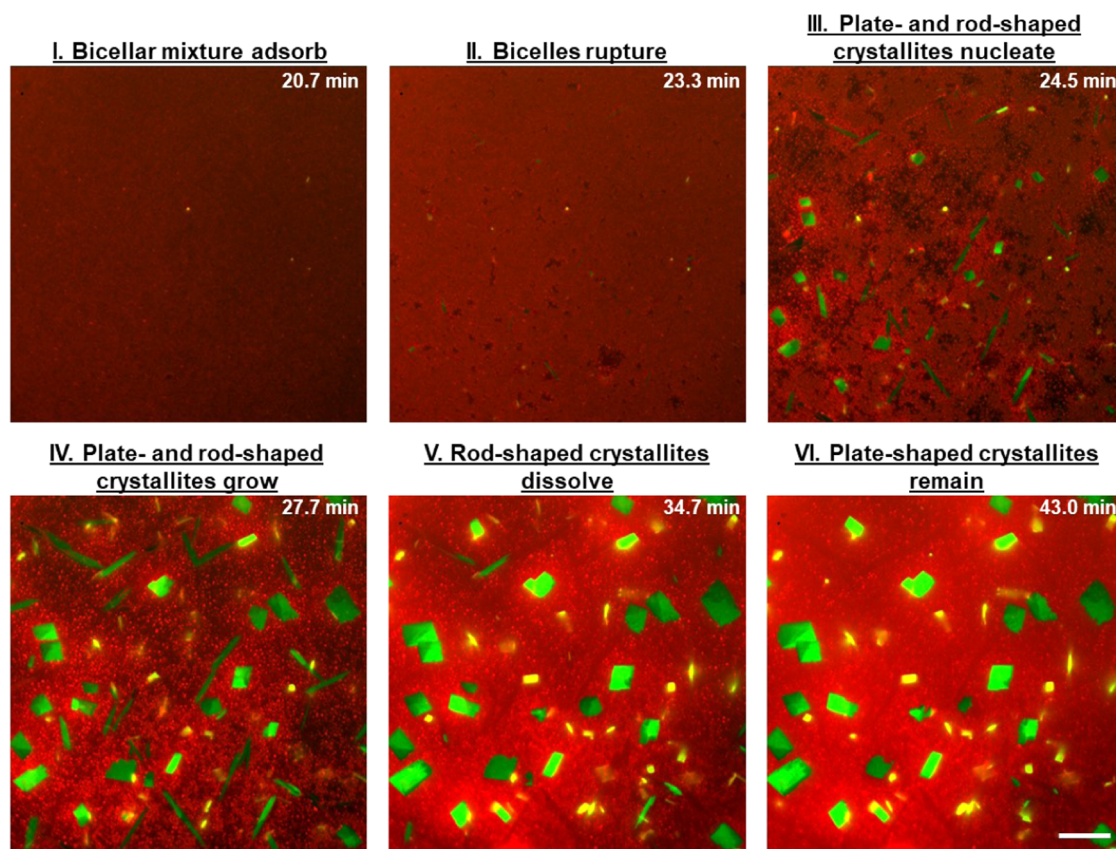


Figure 2. Time-lapsed images of the adsorption of 80 mol % cholesterol-containing bicellar mixture labeled with Rh-PE (red) and BODIPY-Chol (green) dyes onto the glass surface and subsequent cholesterol crystallite growth were recorded by epifluorescence microscopy experiments. The red and green channels are merged and presented together. The entire adsorption process was classified into the same steps I–VI as in Figure 1. The bicellar mixture was added at $t = 0$ min. The scale bar is 20 μm .

the bicellar mixture with a long-chain lipid concentration of 0.031 mM.

Epifluorescence Microscopy. Imaging experiments were conducted using a Nikon Eclipse Ti-E inverted microscope with a 60 \times oil-immersion objective (NA 1.49) and a mercury-fiber illuminator C-HGFIE Intensilight (Nikon, Tokyo, Japan) excitation source. The light was passed through an alternating dichroic filter block (Ex 480/40, Em 535/50) or (Ex 545/30, Em 605/70) for imaging in the green and red channels. An Andor iXon3 897 EMCCD camera was used to obtain the images at 1 frame per 3 s. The experiments were conducted within a flow-through, microfluidic chamber consisting of a bottomless slide (sticky-Slide VI 0.4, ibidi GmbH, Martinsried, Germany) mounted onto a glass coverslip, and liquid samples were introduced at a flow rate of 100 $\mu\text{L}/\text{min}$, as controlled by a peristaltic pump. All measurements were conducted at room temperature (~ 25 $^{\circ}\text{C}$).

Quartz Crystal Microbalance with Dissipation (QCM-D). QCM-D experiments were conducted using a Q-Sense E4 instrument (Biolin Scientific AB, Stockholm, Sweden) and silica-coated AT-cut quartz crystal sensor chips with a fundamental frequency of 5 MHz (QSX 303, Biolin Scientific). Prior to each experiment, the quartz crystal sensor chips were sequentially rinsed with water and then ethanol, followed by drying under a gentle stream of nitrogen gas and then treated with oxygen plasma (PDC-002, Harrick Plasma, Ithaca, NY) for 1 min. The temperature of the QCM-D chamber was maintained at 25 $^{\circ}\text{C}$. All solutions were added under continuous flow conditions using a peristaltic pump (Reglo Digital, Ismatec, Glattbrugg, Switzerland) with a flow rate of 100 $\mu\text{L}/\text{min}$. The resonance frequency (Δf) and energy dissipation (ΔD) shifts were recorded in real time at multiple odd overtones by the Q-Soft software package (Biolin Scientific AB).

RESULTS AND DISCUSSION

Formation of Cholesterol Crystallites in an SLB. Our methodology to fabricate cholesterol crystallites in a model membrane is based on the well-established method of forming SLBs via adsorption, rupture, and fusion of bicelles, which are self-assembled disklike nanostructures.^{31–33} In the present case, we prepared a lipid mixture consisting of long-chain (20 mol % DOPC and 80 mol % cholesterol) and short-chain (DHPC) lipids. The concentration of short-chain lipids is 4 times that of the total long-chain lipid concentration (q -ratio 0.25). Crystal growth is driven by supersaturation, and indeed, 80 mol % cholesterol is above the solubility limit of cholesterol in a phosphatidylcholine (PC) bilayer (~ 66 mol %).³⁴ Therefore, it is likely that this bicellar mixture contains not only conventional bicelles but also various types of cholesterol-associated lipid aggregates, possibly including tiny cholesterol seed crystals.²⁰ Indeed, previous dynamic light scattering measurements revealed that the bicellar mixture possessed a multimodal size distribution with peaks at around 50, 1000, and 2000 nm.²⁴

In our present experiments, the cholesterol-rich bicellar mixture with a long-chain lipid concentration of 0.031 mM was adsorbed onto a glass or silica surface (Figure 1). Upon reaching a critical coverage, the adsorbed bicelles in the bicellar mixture ruptured and fused, causing the highly soluble DHPC lipids to escape into the bulk solution, thus forming an SLB. Thereafter, the nucleation and eventual growth of three-dimensional (3D) cholesterol crystallites were observed within

the SLB. We note here that nucleation could possibly occur in two ways. In one way, the cholesterol seed crystals that were formed in the solution phase within the bicellar mixture were adsorbed onto the surface and then served as nucleation sites. In another way, nucleation occurs on the surface from within the SLB due to cholesterol supersaturation. In either case, nucleation and growth are likely aided by the diffusion and transport of cholesterol molecules within the SLB.

Epifluorescence Microscopy. Time-lapsed epifluorescence microscopy imaging allowed us to visually observe the adsorption of the bicellar mixture containing 80 mol % cholesterol onto a glass surface, which leads to the formation of an SLB and subsequent spontaneous cholesterol crystallite growth. The bicellar mixture was labeled with Rh-PE and BODIPY-Chol dyes to allow for fluorescence imaging of the DOPC and cholesterol molecules in red and green channels, respectively. The sample was injected into a microfluidic chamber, and the initial injection time was defined as $t = 0$ min. Images with merged red and green channels taken at various time points during the experiment are presented in Figure 2. Six distinct steps were identified based on the obtained fluorescence micrographs: (I) the adsorption of the cholesterol-rich bicellar mixture, (II) rupture of the bicelles and SLB formation, (III) nucleation of cholesterol crystallites, (IV) growth of 3D cholesterol crystallites with rod- and plate-shaped morphologies, (V) dissolution of rod-shaped crystallites and growth of plate-shaped crystallites, and finally (VI) a majority of plate-shaped crystallites remaining nearly at the equilibrium.

During the first 20 min after the initial injection, the fluorescence intensity in both channels gradually increased, indicating the adsorption of the bicellar mixture onto the glass surface (step I). At around $t = 23.3$ min, the adsorbed bicellar mixture reached critical coverage, ruptured, and formed a cholesterol-rich SLB (step II). The onset of cholesterol crystallite nucleation was observable by $t = 24.5$ min, as indicated by the appearance of several micrometer-sized crystal habits in the green channel with low and high aspect ratios (step III). Indeed, cholesterol crystals can take on diverse shapes,³⁵ including plate- and rod-like morphologies, which correspond to the energetically stable triclinic and less stable monoclinic crystal structures, respectively.^{22,36–39} Accordingly, we have termed the observed cholesterol crystallites with low and high aspect ratios as plate-shaped and rod-shaped crystallites, respectively.

After nucleation, the crystallites exhibited a steady increase in size over time. Interestingly, the rod-shaped crystallites grew to a maximum size at around $t = 27.7$ min (step IV), after which they started to reduce in size, eventually leading to the complete disappearance of many rod-shaped crystallites at $t = 34.7$ min (step V). On the other hand, the plate-shaped crystallites continued to grow rapidly in size during this time. These observations suggest the occurrence of an Ostwald ripening effect, in which the rod-shaped crystallites dissolved and cholesterol molecules likely redeposited onto the plate-shaped crystallites.⁴⁰ Although it has been proposed in the literature that rod-shaped monoclinic cholesterol monohydrate crystals that grow within lipid membranes transform into plate-shaped triclinic crystals,^{23,36,37} this was not observed in our experiments. By $t = 43.0$ min, the overall cholesterol monohydrate crystal population largely consisted of plate-shaped crystallites (step VI).

Ostwald Ripening. Cholesterol crystallization under biologically relevant conditions has long attracted attention (see, e.g., refs 22, 41–43). Also, many experimental and theoretical studies have been focused on the formation and Ostwald ripening of cholesterol rafts in lipid bilayers in the past decade (see, e.g., refs 44, 45). The kinetic models used in the former studies are, however, not well developed, whereas the kinetic models employed in the latter studies are not directly applicable to our case. In all of these models, cholesterol crystallites are assumed to be of one type. In particular, the former models usually describe the formation and growth of fat (cholesterol) crystallites in terms of one-phase models, e.g., of the Avrami–Kolmogorov–Johnson–Mehl or other types (refs 46, 47). In fact, such models are focused on the growth rather than on Ostwald ripening of crystallites. To articulate the specifics of the Ostwald ripening we observe, it is instructive to recall the conventional scheme of this process. In general, during Ostwald ripening, the growth of larger aggregates occurs at the expense of smaller ones via detachment, diffusion, and attachment of monomers. Usually, the phase state of aggregates is the same, the concentration of monomers is close to equilibrium, the evolution of a single aggregate is considered to be controlled by diffusion of monomers, and the equation for the aggregate size (radius) is represented as⁴⁸

$$\frac{dR}{dt} = \frac{AD}{R} \left(\frac{1}{\langle R \rangle} - \frac{1}{R} \right) \quad (1)$$

where D is the monomer diffusion coefficient, $\langle R \rangle$ is the average size of the aggregates, and A is a constant dependent on the aggregate surface tension (to be specific, we refer to the Lifshitz–Slyozov scenario of ripening in solution). The evolution of $\langle R \rangle$ is asymptotically described by the power law

$$\langle R \rangle = (\langle R \rangle_0^n + Bt)^{1/n} \quad (2)$$

where $\langle R \rangle_0$ is the initial $\langle R \rangle$ value and B and n are the parameters dependent on the details of the kinetics. For the Lifshitz–Slyozov scenario, the theory predicts $n = 3$. Another important example is sintering supported metal nanoparticles, where the process can be controlled by monomer attachment to particles at the metal–support interface, namely, the attachment itself (interface controlled regime) or diffusion of monomers across the support (diffusion-controlled regime), and n is predicted to be 3 or 4, respectively (see, e.g., ref 49 and references therein).

In our case, the initial steps (I–III) of phase transition include the formation of two aggregate phases, including 3D rod- and plate-shaped cholesterol crystallites. Ostwald ripening takes place during steps IV and VI. In particular, the growth of plate-shaped crystallites occurs at the expense of rod-shaped crystallites because the latter are thermodynamically less stable. To illustrate what may happen in this case, we consider that the rod-shaped crystallites lose mass at their terminal sides at a constant rate and, focusing on step IV, assume that the surface concentrations of crystallites are, in this case, approximately constant. In this scenario, the rate of the gain of mass by each plate-shaped crystallite is constant as well, and the equation for the effective size of these crystallites can be represented as

$$4\pi\rho\langle R \rangle^2 \frac{d\langle R \rangle}{dt} = w \quad (3)$$

where ρ is the cholesterol density and w is the average mass-supply rate (per crystallite) dependent on the mass-transport

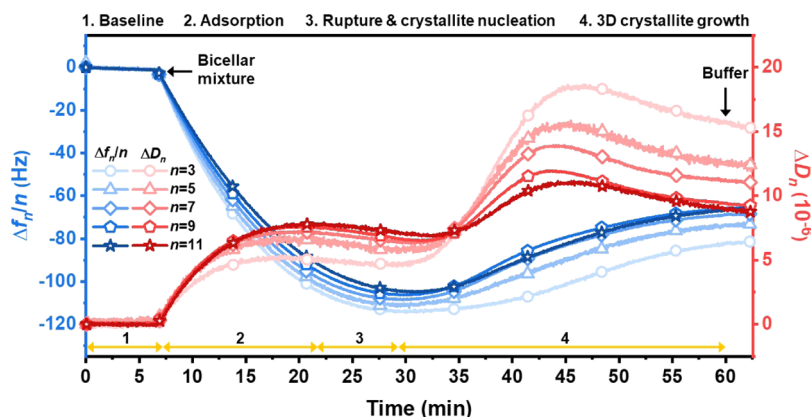


Figure 3. $\Delta f_n/n$ and ΔD_n values from the 3rd to 11th overtone (n) from QCM-D measurements of the adsorption of the 80 mol % cholesterol-containing bicellar mixture on a silica surface and subsequent cholesterol crystallite growth were recorded as a function of time. The entire adsorption process was classified into four stages. (1) Baseline in the buffer solution. (2) Adsorption of the bicellar mixture onto the silica surface. (3) Rupture of the bicelles and the onset of cholesterol crystallite nucleation. (4) Formation of 3D cholesterol crystallites. The stable baseline in the buffer solution was first established followed by the introduction of the bicellar mixture into the measurement chamber at around $t = 7$ min. A washing step with the buffer solution was then conducted at around $t = 60$ min.

rate and the ratio of the concentrations of the rod- and plate-shaped crystallites. If w is constant (as we assume), the integration of eq 3 results in the power-law kinetics with $n = 3$ (as in the Lifshitz–Slyozov case). This generic analysis shows that the Ostwald ripening kinetics can be apparently similar despite quite different mechanistic details. Our experiments allow us to clarify the mechanistic aspects of Ostwald ripening in the case under consideration but, unfortunately, do not allow us to fully quantify the growth of plate-shaped crystallites and to determine n .

To clarify whether the mass transport along the surface is sufficiently fast for the Ostwald ripening described above, it is instructive to estimate the average length, $l = (4Dt)^{1/2}$, of 2D diffusion of cholesterol or lipids in an SLB (D is the diffusion coefficient). According to our earlier study,²⁴ the scale of D is $2.5 \mu\text{m}^2/\text{s}$. We may assume that both cholesterol and phospholipid molecules in the SLB have similar diffusivities.^{50,51} With this value of D and the scale of t as 20 min, we have $l \approx 110 \mu\text{m}$. By contrast, the average distance between a rod-shaped and plate-shaped crystallite appears to be within $20 \mu\text{m}$. Based on these values, it appears that the mass transport along the SLB surface is sufficiently rapid for Ostwald ripening.

Quartz Crystal Microbalance with Dissipation. To analyze further the cholesterol crystallite growth process, we next conducted QCM-D experiments at five different overtones ($n = 3, 5, 7, 9,$ and 11) and monitored the adsorption kinetics of the 80 mol % cholesterol bicellar mixture on silica surfaces (Figure 3). In general, negative shifts in the resonance frequency normalized to the corresponding overtone ($\Delta f_n/n$) correspond to an increase in the mass of an adsorbing species, and positive energy dissipation shifts (ΔD_n) correspond to an increase in the viscoelastic character of the adsorbing species. Both signal readouts are also sensitive to the hydrodynamically coupled solvent surrounding the adsorbates. Concerning the relation of the QCM-D kinetics to the patterns shown in Figure 2, we note that the QCM-D measurement chamber differs from the one used for epifluorescence microscopy and that QCM-D measurements are ensemble-averaged. Hence, although the results from the two experiments should not be directly compared, their sequence of events can be broadly associated. Based on the epifluorescence microscopy experiments and the profiles of the QCM-D kinetics, we have

identified and defined the QCM-D data into stages 1–4 within certain time periods, as illustrated by the yellow arrows in Figure 3. Stages 1–4 of the QCM-D data can be associated with steps I–VI from epifluorescence microscopy experiments. Stages 1 and 2 (baseline and adsorption) correspond to step I, stage 3 (rupture and crystallite nucleation) corresponds to steps II and III, and stage 4 (3D crystallite growth) corresponds to steps IV–VI. After establishing a stable baseline signal in buffer solution (stage 1), we injected the bicellar mixture at around $t = 7$ min (stage 2), following which negative $\Delta f_n/n$ and positive ΔD_n shifts were observed for all overtones. During adsorption, $\Delta f_n/n$ and ΔD_n values became n -dependent and both yielded more positive values at higher overtones, which is typically observed for the adsorption of nonrigid films, such as a single layer of intact lipid vesicles.^{52,53}

At around $t = 22$ min, the ΔD_n kinetics showed a gentle peak, reaching values of about 5.0×10^{-6} , 6.5×10^{-6} , 7.1×10^{-6} , 7.5×10^{-6} , and 7.7×10^{-6} for $n = 3, 5, 7, 9,$ and 11 , respectively, while the $\Delta f_n/n$ kinetics showed a continued decrease, with values of about -104.3 , -101.4 , -98.2 , -95.2 , and -91.9 Hz for $n = 3, 5, 7, 9,$ and 11 , respectively. These kinetics can be compared to our previously reported observations for the adsorption and rupture of the 60 mol % cholesterol-containing bicellar mixture.⁵⁴ We note that in the 60 mol % cholesterol case, a maximum ΔD_n accompanied by a minimum $\Delta f_n/n$ corresponds to the rupture and fusion of bicelles in the bicellar mixture, which supports that a similar case has happened for the 80 mol % cholesterol bicellar mixture and that an SLB has been formed on the silica surface (stage 3). However, the 80 mol % cholesterol case here shows a continued negative shift in $\Delta f_n/n$ rather than a minimum, which supports that the onset of cholesterol crystallite nucleation and growth began immediately upon membrane formation, likely from the cholesterol seed crystals in the bicellar mixture as well as from nucleation within the cholesterol-rich SLB. These kinetics also indicate that crystallite nucleation and growth result in an overall increase in the mass of the adlayer after SLB formation, which suggests that additional cholesterol molecules required for cholesterol crystallite growth are supplied, at least, in part, by the adsorbing bicellar mixture from the bulk solution. At $t = 28$ min, ΔD_n values decreased very slightly to 4.6×10^{-6} , $5.9 \times$

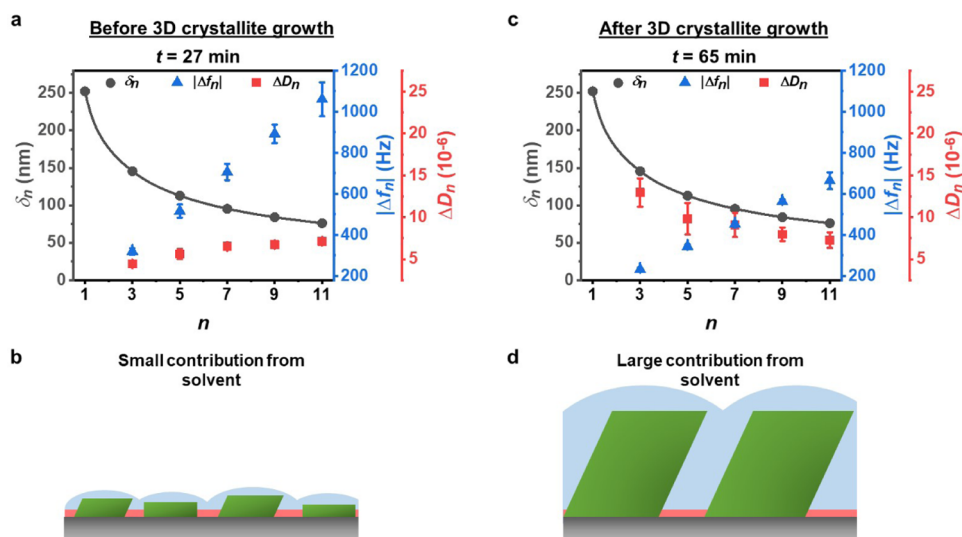


Figure 4. Comparison of the theoretically calculated QCM-D penetration length in water (δ_n) with the experimentally obtained $|\Delta f_n|$ and ΔD_n values (a) at $t = 27$ min (end of stage 3) when the SLB had formed and cholesterol crystallite nucleation had just begun and (c) at $t = 65$ min (end of stage 4) when 3D cholesterol crystallites had fully formed as a function of n . Representative schematic illustrations on the relative extent of solvent contribution (blue shaded areas) to the QCM-D signal response from cholesterol crystallites (green quadrilaterals) in the SLB (red band) are shown in panels (b) and (d), which corresponds to the data in (a) and (c), respectively. Error bars in (a) and (c) represent standard deviations from triplicate QCM-D measurements.

10^{-6} , 6.5×10^{-6} , 6.8×10^{-6} , and 7.3×10^{-6} for $n = 3, 5, 7, 9$, and 11 , respectively, while $\Delta f_n/n$ reached a minimum with values of -113.6 , -110.6 , -107.9 , -105.6 , and -103.6 Hz for $n = 3, 5, 7, 9$, and 11 , respectively. The decrease in $\Delta f_n/n$ values indicates that the cholesterol crystallite nuclei have grown to form small 3D crystallites, thereby contributing to the increased mass of the adlayer. Shortly thereafter, positive shifts in ΔD_n values were observed for all overtones, with the lower overtones reaching a larger magnitude than the higher overtones. $\Delta f_n/n$ values also began to show positive shifts and more pronounced n dependence. This kinetics suggests the onset of 3D cholesterol crystallite growth (stage 4), which follows after the rupture of the bicellar mixture, SLB formation, and cholesterol crystallite nucleation. At around $t = 45$ min, ΔD_n displayed a second maximum while $\Delta f_n/n$ continued to exhibit positive shift kinetics. This feature is consistent with the next morphological change observed from epifluorescence microscopy which is the Ostwald ripening effect where the rod-shaped crystallites shrink and dissolve while plate-shaped crystallites continue to grow. Both $\Delta f_n/n$ and ΔD_n kinetics level off toward the end, indicating that the system was approaching equilibrium as growth of the plate-shaped crystallites started to slow and the rod-shaped crystallites were nearly completely dissolved.

To clarify the n -dependent QCM-D kinetics, it is instructive to recall two limiting cases, allowing well-established analytical descriptions.⁵⁵ The first one involves the firm adsorption of a nondeformable adsorbate on the surface of the QCM-D sensor in vacuum or solution. In this case, the adsorbate contribution to the dissipation is negligible, whereas the contribution to the frequency shift is given by the Sauerbrey expression⁵⁶

$$\Delta f_n = -Cnm_a \quad (4)$$

where m_a is the adsorbate mass (per unit area) and C is the mass sensitivity constant. The second case encompasses situations when the QCM-D sensor interacts with the solvent in the absence of an adsorbate. In the latter case, the

penetration length of QCM-induced oscillations, δ_n (Figure 4) and the solvent-related frequency and dissipation shifts are described as

$$\delta_n = \left(\frac{\eta_s}{\pi n \rho_s f_F} \right)^{1/2} \quad (5)$$

$$\Delta f_n = -C \left(\frac{n \rho_s \eta_s}{4\pi f_F} \right)^{1/2} \quad (6)$$

$$\Delta D_n = C \left(\frac{\rho_s \eta_s}{\pi n f_F^3} \right)^{1/2} \quad (7)$$

where f_F is the fundamental resonance frequency and η_s and ρ_s are the solution viscosity and density, respectively. Qualitatively, $|\Delta f_n|$ increases, while ΔD_n and δ_n decrease as a function of n for a given system where the contribution of solvent predominates.

In biologically relevant situations, the adsorbed species are deformable and at appreciable coverage can usually be viewed as a geometrically heterogeneous film including solvent (water). In such situations, the adsorbate contribution to Δf_n can often still be estimated by eq 4. The contribution of the solvent located above a film to Δf_n and ΔD_n can roughly be estimated by eqs 6 and 7 as well, and the latter expressions are in fact taken into account by associating the baseline signal with that corresponding to the QCM-D sensor in solution. The contribution of the solvent trapped inside a film to Δf_n and ΔD_n depends on the ratio between δ_n and the length scale, characterizing the space between adjacent adsorbed species, and in general can hardly be accurately described theoretically, especially in the cases of aggregates with sizes comparable with δ_n . In principle, such heterogeneous films can be described by employing the Voigt–Voinova model designed for homogeneous viscoelastic films,⁵⁷ but in this case, the interpretation of

the corresponding parameters is often not straightforward because this model ignores system heterogeneity [such as the time-dependent growth and shape evolution of the 3D cholesterol crystallites (including Ostwald ripening) as we have in our case]. One of the analytical approaches allowing one to describe phenomenologically heterogeneous films in terms of porosity is based on the use of Brinkman's mean-field 1D equation for porous films.⁵⁸ The porosity can, however, hardly be accurately calculated in real biologically relevant situations. There are also numerical calculations corresponding to specific adsorbate geometries (see, e.g., ref 59 and references therein). Such results are, however, not universal and nowadays can hardly be used to describe the kinetics.

In our analysis of the present QCM-D results, we instead use an approach based partly on eqs 4–7 and partly on earlier experimental results obtained for relatively simple systems. We note that during adsorption of the cholesterol-rich bicellar mixture, rupture of the adsorbed cholesterol-rich aggregates (e.g., bicelles), and crystallite nucleation (stages 2 and 3 in Figure 3), the adsorbed overlayer can be considered to be close to close-packed as evident from the weak dependence of $\Delta f_n/n$ and ΔD_n on n . Additionally, at the end of stage 3 ($t = 27$ min), both $|\Delta f_n|$ and ΔD_n increase with increasing n (Figure 4a). The former is in agreement with eq 6, while the latter is opposite compared to eq 7. Taken together, these trends support that the contribution of the solvent to the observed QCM-D signal readout at this stage is minor (Figure 4b). To estimate the film thickness at the end of stage 3, we use $|\Delta f_n/n| = 105$ Hz and for comparison note that $|\Delta f_n/n| = 26$ Hz for an SLB (see, e.g., ref 60). Furthermore, taking into account that the SLB thickness is 4.5 nm, we can estimate the film thickness as $l_f \approx 4.5 \times 105/26 \approx 18$ nm. While this thickness value at this stage is much smaller compared with δ_n , it is larger than that of a conventional SLB, which is consistent with the presence of additional cholesterol-associated aggregates or cholesterol crystallite nuclei within the SLB, which have average characteristic sizes larger than the thickness of a bilayer (cf. dynamic light scattering measurements in ref 24).

Beginning at around $t = 30$ min, the formation of 3D cholesterol crystallites occurs and the dependence of both $\Delta f_n/n$ and ΔD_n on n is somewhat stronger (stage 4 in Figure 3). With increasing time, $|\Delta f_n/n|$ decreases and ΔD_n eventually decreases as well. The former is observed from the beginning of stage 4 and appears to be indicative of some loss of the cholesterol mass. The latter can partly be related to the increase and subsequent decrease in the amount of trapped water with the growth and subsequent disappearance of the rod-shaped crystallites and partly to the loss of the cholesterol mass as well. At the end of stage 4 ($t = 65$ min), both $|\Delta f_n|$ and ΔD_n are in qualitative agreement with eqs 6 and 7 (Figure 4c). This seems to mean that the role of the trapped solvent becomes larger as expected when taking into account that in this case the cholesterol crystallites are well separated (Figure 4d).

We also note here that our observed QCM-D results may be reminiscent of an "elastic loading" regime, where specific contact mechanics of large adsorbing species produces positive $\Delta f_n/n$.^{61–64} However, it is unlikely that this scenario can be applicable in our present case as the size of the cholesterol crystallites appreciably changes with increasing time, and thus, the corresponding $\Delta f_n/n$ and ΔD_n would be expected to dramatically depend on time and n . The effects we observe here are, however, comparatively very modest.

To estimate roughly the height of the cholesterol crystallites in the end of stage 4, which are predominately plate-shaped at this stage, we can consider that they occupy $\sim 10\%$ of the surface (based on ImageJ analysis of epifluorescence micrographs) and the corresponding QCM-D $|\Delta f_n/n|$ is ~ 70 Hz. Then, by analogy with the estimate above, the plate-shaped crystallite height is given by $4.5 \times 70/26/0.1 \approx 120$ nm. It is of interest that the latter value is comparable with δ_n . This means that although the attenuation of the QCM-induced oscillations in solution is not negligible in this case, its role is not dramatic. Concerning the fraction of the surface covered by crystallites, $\sim 10\%$, and thickness, ~ 120 nm, it is of interest to note that in the case of SiO₂ nanoparticles with a diameter of ~ 140 nm⁶⁵ and polystyrene latex nanoparticles with a diameter of ~ 110 nm⁶⁶ with comparable surface coverages, the scale of ΔD_n is comparable to that measured in our case. This is in favor of our conclusion that the dissipation is related primarily to trapped water (the internal dissipation is negligible in the SiO₂ case).

CONCLUSIONS

In this study, we presented an analysis of the fabrication of an SLB and the growth of 3D cholesterol crystallites from the adsorption of the 80 mol % cholesterol bicellar mixture onto a glass and silica surface and monitored in situ by epifluorescence microscopy and QCM-D experiments. Based on the visual observations from epifluorescence microscopy experiments, we classified the entire process into six steps: (I) adsorption of the cholesterol-rich bicellar mixture, (II) rupture of bicelles in the bicellar mixture leading to SLB formation, (III) nucleation of the cholesterol crystallites, (IV) growth of rod- and plate-shaped 3D cholesterol crystallites, (V) shrinking and dissolution of rod-shaped crystallites, and finally (VI) a nearly equilibrium state consisting mostly of plate-shaped crystallites. The cholesterol crystallite nuclei grew into two distinct micrometer-scale morphologies that possessed a high- and a low-aspect-ratio crystal habit, termed as rod-shaped and plate-shaped crystallites, which correspond to monoclinic and triclinic crystal structures, respectively. Ostwald ripening behavior was observed in steps IV–VI, whereby the rod-shaped crystallites shrank, while the plate-shaped crystallites grew and that showed apparent similarities with the Lifshitz–Slyozov scenario of ripening in solution. Its qualitatively new feature is that the aggregates of one phase grow at the expense of the aggregates of the other phase. We classified the associated QCM-D kinetics into four stages: (1) buffer baseline, (2) adsorption of the bicellar mixture, (3) rupture and crystallite nucleation, and (4) 3D crystallite growth. Based on the n dependence of the QCM-D data, we scrutinized the effect of the solvent trapped between the 3D cholesterol crystallites. Our analysis based on the fundamental principles of QCM-D interactions in solution as well as comparisons with relatively simpler reference systems qualitatively supports our observations.

Taken together, our findings revealed fundamental mechanistic details of our methodology of fabricating cholesterol crystallites within an SLB from the adsorption of the cholesterol-rich bicellar mixture and provide the groundwork for future studies to develop and optimize our methodology for enhanced bioanalytical and clinical diagnostic applications in the area under consideration.

AUTHOR INFORMATION

Corresponding Author

Nam-Joon Cho – School of Materials Science and Engineering,
Nanyang Technological University, 639798, Singapore;
orcid.org/0000-0002-8692-8955; Email: njcho@ntu.edu.sg

Authors

Gamaliel Junren Ma – School of Materials Science and Engineering,
Nanyang Technological University, 639798, Singapore; orcid.org/0000-0002-6740-1031

Vladimir P. Zhdanov – Boreskov Institute of Catalysis,
Russian Academy of Sciences, Novosibirsk 630090, Russia

Soohyun Park – School of Materials Science and Engineering,
Nanyang Technological University, 639798, Singapore;
orcid.org/0000-0003-3261-7585

Tun Naw Sut – School of Materials Science and Engineering,
Nanyang Technological University, 639798, Singapore

Complete contact information is available at:

<https://pubs.acs.org/10.1021/acs.langmuir.1c00174>

Notes

The authors declare no competing financial interest.

ACKNOWLEDGMENTS

This work was supported by the National Research Foundation of Singapore through a Competitive Research Programme grant (NRF-CRP10-2012-07) and a Proof-of-Concept grant (NRF2015NRF-POC0001-19).

REFERENCES

- (1) Yeagle, P. L. Cholesterol and the cell membrane. *Biochim. Biophys. Acta* **1985**, *822*, 267–287.
- (2) McMullen, T. P.; Lewis, R. N.; McElhaney, R. N. Cholesterol–phospholipid interactions, the liquid-ordered phase and lipid rafts in model and biological membranes. *Curr. Opin. Colloid Interface Sci.* **2004**, *8*, 459–468.
- (3) Van Meer, G.; Voelker, D. R.; Feigenson, G. W. Membrane lipids: where they are and how they behave. *Nat. Rev. Mol. Cell Biol.* **2008**, *9*, 112–124.
- (4) Ohvo-Rekilä, H.; Ramstedt, B.; Leppimäki, P.; Slotte, J. P. Cholesterol interactions with phospholipids in membranes. *Prog. Lipid Res.* **2002**, *41*, 66–97.
- (5) Widomska, J.; Subczynski, W. K. Why Is Very High Cholesterol Content Beneficial for the Eye Lens but Negative for Other Organs? *Nutrients* **2019**, *11*, No. 1083.
- (6) Mason, R. P.; Tulenko, T. N.; Jacob, R. F. Direct evidence for cholesterol crystalline domains in biological membranes: role in human pathobiology. *Biochim. Biophys. Acta* **2003**, *1610*, 198–207.
- (7) Sedaghat, A.; Grundy, S. M. Cholesterol crystals and the formation of cholesterol gallstones. *N. Engl. J. Med.* **1980**, *302*, 1274–1277.
- (8) Wang, D. Q.; Cohen, D. E.; Carey, M. C. Biliary lipids and cholesterol gallstone disease. *J. Lipid Res.* **2009**, *50*, S406–S411.
- (9) Duewell, P.; Kono, H.; Rayner, K. J.; Sirois, C. M.; Vladimer, G.; Bauernfeind, F. G.; Abela, G. S.; Franchi, L.; Nuñez, G.; Schnurr, M.; et al. NLRP3 inflammasomes are required for atherogenesis and activated by cholesterol crystals. *Nature* **2010**, *464*, 1357–1361.
- (10) Abela, G. S. Cholesterol crystals piercing the arterial plaque and intima trigger local and systemic inflammation. *J. Clin. Lipidol.* **2010**, *4*, 156–164.
- (11) Pang, C. E.; Messinger, J. D.; Zanzottera, E. C.; Freund, K. B.; Curcio, C. A. The Onion Sign in Neovascular Age-Related Macular Degeneration Represents Cholesterol Crystals. *Ophthalmology* **2015**, *122*, 2316–2326.
- (12) Cantuti-Castelvetri, L.; Fitzner, D.; Bosch-Queralt, M.; Weil, M.-T.; Su, M.; Sen, P.; Ruhwedel, T.; Mitkovski, M.; Trendelenburg, G.; Lütjohann, D.; et al. Defective cholesterol clearance limits remyelination in the aged central nervous system. *Science* **2018**, *359*, 684–688.
- (13) Chan, Y.-H. M.; Boxer, S. G. Model membrane systems and their applications. *Curr. Opin. Chem. Biol.* **2007**, *11*, 581–587.
- (14) Sanders, C. R.; Prosser, R. S. Bicelles: a model membrane system for all seasons? *Structure* **1998**, *6*, 1227–1234.
- (15) Jackman, J. A.; Knoll, W.; Cho, N.-J. Biotechnology applications of tethered lipid bilayer membranes. *Materials* **2012**, *5*, No. 2637.
- (16) Jackman, J. A.; Cho, N.-J. Model membrane platforms for biomedicine: case study on antiviral drug development. *Biointerphases* **2012**, *7*, No. 18.
- (17) Jackman, J. A.; Cho, N.-J. Supported Lipid Bilayer Formation: Beyond Vesicle Fusion. *Langmuir* **2020**, *36*, 1387–1400.
- (18) Hardy, G. J.; Nayak, R.; Zauscher, S. Model cell membranes: Techniques to form complex biomimetic supported lipid bilayers via vesicle fusion. *Curr. Opin. Colloid Interface Sci.* **2013**, *18*, 448–458.
- (19) Ziblat, R.; Leiserowitz, L.; Addadi, L. Crystalline domain structure and cholesterol crystal nucleation in single hydrated DPPC: cholesterol: POPC bilayers. *J. Am. Chem. Soc.* **2010**, *132*, 9920–9927.
- (20) Mainali, L.; Raguz, M.; Subczynski, W. K. Formation of cholesterol bilayer domains precedes formation of cholesterol crystals in cholesterol/dimyristoylphosphatidylcholine membranes: EPR and DSC studies. *J. Phys. Chem. B* **2013**, *117*, 8994–9003.
- (21) Barrett, M. A.; Zheng, S.; Topozini, L. A.; Alsop, R. J.; Dies, H.; Wang, A.; Jago, N.; Moore, M.; Rheinstädter, M. C. Solubility of cholesterol in lipid membranes and the formation of immiscible cholesterol plaques at high cholesterol concentrations. *Soft Matter* **2013**, *9*, 9342–9351.
- (22) Varsano, N.; Fargion, I.; Wolf, S. G.; Leiserowitz, L.; Addadi, L. Formation of 3D cholesterol crystals from 2D nucleation sites in lipid bilayer membranes: implications for atherosclerosis. *J. Am. Chem. Soc.* **2015**, *137*, 1601–1607.
- (23) Varsano, N.; Beghi, F.; Dadosh, T.; Elad, N.; Pereiro, E.; Haran, G.; Leiserowitz, L.; Addadi, L. The Effect of the Phospholipid Bilayer Environment on Cholesterol Crystal Polymorphism. *ChemPlusChem* **2019**, *84*, 338–344.
- (24) Park, S.; Sut, T. N.; Ma, G. J.; Parikh, A. N.; Cho, N.-J. Crystallization of Cholesterol in Phospholipid Membranes Follows Ostwald's Rule of Stages. *J. Am. Chem. Soc.* **2020**, *142*, 21872–21882.
- (25) Jackman, J. A.; Ferhan, A. R.; Cho, N.-J. Surface-based nanoplasmonic sensors for biointerfacial science applications. *Bull. Chem. Soc. Jpn.* **2019**, *92*, 1404–1412.
- (26) Dacic, M.; Jackman, J. A.; Yorulmaz, S.; Zhdanov, V. P.; Kasemo, B.; Cho, N.-J. Influence of divalent cations on deformation and rupture of adsorbed lipid vesicles. *Langmuir* **2016**, *32*, 6486–6495.
- (27) Jackman, J. A.; Avsar, Y.; Ferhan, S.; Li, A. R.; Park, D.; Zhdanov, J. H.; Cho, V. P. N.-J., Quantitative profiling of nanoscale liposome deformation by a localized surface plasmon resonance sensor. *Anal. Chem.* **2017**, *89*, 1102–1109.
- (28) Yoon, B. K.; Park, H.; Zhdanov, V. P.; Jackman, J. A.; Cho, N.-J. Real-time nanoplasmonic sensing of three-dimensional morphological changes in a supported lipid bilayer and antimicrobial testing applications. *Biosens. Bioelectron.* **2021**, *174*, No. 112768.
- (29) Gillissen, J. J.; Tabaei, S. R.; Jackman, J. A.; Cho, N.-J. A model derived from hydrodynamic simulations for extracting the size of spherical particles from the quartz crystal microbalance. *Analyst* **2017**, *142*, 3370–3379.
- (30) Adamczyk, Z.; Sadowska, M. Hydrodynamic Solvent Coupling Effects in Quartz Crystal Microbalance Measurements of Nanoparticle Deposition Kinetics. *Anal. Chem.* **2020**, *92*, 3896–3903.
- (31) Kolahdouzan, K.; Jackman, J. A.; Yoon, B. K.; Kim, M. C.; Johal, M. S.; Cho, N.-J. Optimizing the formation of supported lipid bilayers from bicellar mixtures. *Langmuir* **2017**, *33*, 5052–5064.

- (32) Sut, T. N.; Jackman, J. A.; Cho, N.-J. Understanding How Membrane Surface Charge Influences Lipid Bicelle Adsorption onto Oxide Surfaces. *Langmuir* **2019**, *35*, 8436–8444.
- (33) Sut, T. N.; Jackman, J. A.; Yoon, B. K.; Park, S.; Kolahdouzan, K.; Ma, G. J.; Zhdanov, V. P.; Cho, N.-J. Influence of NaCl concentration on bicelle-mediated SLB formation. *Langmuir* **2019**, *35*, 10658–10666.
- (34) Huang, J.; Buboltz, J. T.; Feigenson, G. W. Maximum solubility of cholesterol in phosphatidylcholine and phosphatidylethanolamine bilayers. *Biochim. Biophys. Acta* **1999**, *1417*, 89–100.
- (35) Konikoff, F.; Chung, D.; Donovan, J.; Small, D.; Carey, M. Filamentous, helical, and tubular microstructures during cholesterol crystallization from bile. Evidence that cholesterol does not nucleate classic monohydrate plates. *J. Clin. Invest.* **1992**, *90*, 1155–1160.
- (36) Weihs, D.; Schmidt, J.; Goldiner, I.; Danino, D.; Rubin, M.; Talmon, Y.; Konikoff, F. M. Biliary cholesterol crystallization characterized by single-crystal cryogenic electron diffraction. *J. Lipid Res.* **2005**, *46*, 942–948.
- (37) Solomonov, I.; Weygand, M. J.; Kjaer, K.; Rapaport, H.; Leiserowitz, L. Trapping crystal nucleation of cholesterol monohydrate: relevance to pathological crystallization. *Biophys. J.* **2005**, *88*, 1809–1817.
- (38) Varsano, N.; Beghi, F.; Elad, N.; Pereiro, E.; Dadosh, T.; Pinkas, I.; Perez-Berna, A. J.; Jin, X.; Kruth, H. S.; Leiserowitz, L.; et al. Two polymorphic cholesterol monohydrate crystal structures form in macrophage culture models of atherosclerosis. *Proc. Natl. Acad. Sci. U.S.A.* **2018**, *115*, 7662–7669.
- (39) Hadley, K.; McCabe, C. A structurally relevant coarse-grained model for cholesterol. *Biophys. J.* **2010**, *99*, 2896–2905.
- (40) Frincu, M. C.; Fleming, S. D.; Rohl, A. L.; Swift, J. A. The epitaxial growth of cholesterol crystals from bile solutions on calcite substrates. *J. Am. Chem. Soc.* **2004**, *126*, 7915–7924.
- (41) Portincasa, P.; Venneman, N. G.; Moschetta, A.; van den Berg, A.; Palasciano, G.; van Erpecum, K. J.; et al. Quantitation of cholesterol crystallization from supersaturated model bile. *J. Lipid Res.* **2002**, *43*, 604–610.
- (42) Wang, H. H.; Portincasa, P.; Wang, D. Molecular pathophysiology and physical chemistry of cholesterol gallstones. *Front. Biosci.* **2008**, *13*, 401–423.
- (43) Nidorf, S. M.; Fiolet, A.; Abela, G. S. Viewing atherosclerosis through a crystal lens: How the evolving structure of cholesterol crystals in atherosclerotic plaque alters its stability. *J. Clin. Lipidol.* **2020**, *14*, 619–630.
- (44) Cebecauer, M.; Amaro, M.; Jurkiewicz, P.; Sarmiento, M. J.; Šachl, R.; Cwiklik, L.; Hof, M. Membrane lipid nanodomains. *Chem. Rev.* **2018**, *118*, 11259–11297.
- (45) Moats, K. A.; Asadi, E.; Laradji, M. Phase field crystal simulations of the kinetics of Ostwald ripening in two dimensions. *Phys. Rev. E* **2019**, *99*, No. 012803.
- (46) Foubert, I.; Dewettinck, K.; Vanrolleghem, P. A. Modelling of the crystallization kinetics of fats. *Trends Food Sci. Technol.* **2003**, *14*, 79–92.
- (47) Siódmiak, J. Gallstone formation as an example of the two-step space confined aggregation process. *BioSystems* **2019**, *176*, 1–5.
- (48) Lifshitz, E. M.; Pitaevski, L. P. Kinetics of Phase Transitions. In *Course of Theoretical Physics*; Lifshitz, E. M.; Pitaevski, L. P., Eds.; Pergamon: Amsterdam, 1981; Vol. 10, pp 427–447.
- (49) Tabib Zadeh Adibi, P.; Zhdanov, V. P.; Langhammer, C.; Grönbeck, H. Transient bimodal particle size distributions during Pt sintering on alumina and silica. *J. Phys. Chem. C* **2015**, *119*, 989–996.
- (50) Orädd, G.; Lindblom, G.; Westerman, P. W. Lateral diffusion of cholesterol and dimyristoylphosphatidylcholine in a lipid bilayer measured by pulsed field gradient NMR spectroscopy. *Biophys. J.* **2002**, *83*, 2702–2704.
- (51) Scheidt, H. A.; Huster, D.; Gawrisch, K. Diffusion of cholesterol and its precursors in lipid membranes studied by ¹H pulsed field gradient magic angle spinning NMR. *Biophys. J.* **2005**, *89*, 2504–2512.
- (52) Granéli, A.; Edvardsson, M.; Höök, F. DNA-based formation of a supported, three-dimensional lipid vesicle matrix probed by QCM-D and SPR. *ChemPhysChem* **2004**, *5*, 729–733.
- (53) Cho, N.-J.; Kanazawa, K. K.; Glenn, J. S.; Frank, C. W. Employing two different quartz crystal microbalance models to study changes in viscoelastic behavior upon transformation of lipid vesicles to a bilayer on a gold surface. *Anal. Chem.* **2007**, *79*, 7027–7035.
- (54) Sut, T. N.; Park, S.; Choe, Y.; Cho, N.-J. Characterizing the Supported Lipid Membrane Formation from Cholesterol-Rich Bicelles. *Langmuir* **2019**, *35*, 15063–15070.
- (55) Reviakine, I.; Johannsmann, D.; Richter, R. P. Hearing What You Cannot See and Visualizing What You Hear: Interpreting Quartz Crystal Microbalance Data from Solvated Interfaces. *Anal. Chem.* **2011**, *83*, 8838–8848.
- (56) Sauerbrey, G. The use of quartz oscillators for weighing thin layers and for microweighing. *Z. Phys.* **1959**, *155*, 206–222.
- (57) Voinova, M. V.; Rodahl, M.; Jonson, M.; Kasemo, B. Viscoelastic acoustic response of layered polymer films at fluid-solid interfaces: continuum mechanics approach. *Phys. Scr.* **1999**, *59*, No. 391.
- (58) Daikhin, L.; Urbakh, M. Effect of surface film structure on the quartz crystal microbalance response in liquids. *Langmuir* **1996**, *12*, 6354–6360.
- (59) Gillissen, J. J.; Jackman, J. A.; Tabaei, S. R.; Cho, N.-J. A numerical study on the effect of particle surface coverage on the quartz crystal microbalance response. *Anal. Chem.* **2018**, *90*, 2238–2245.
- (60) Jackman, J. A.; Choi, J.-H.; Zhdanov, V. P.; Cho, N.-J. Influence of osmotic pressure on adhesion of lipid vesicles to solid supports. *Langmuir* **2013**, *29*, 11375–11384.
- (61) Berglin, M.; Olsson, A.; Elwing, H. The interaction between model biomaterial coatings and nylon microparticles as measured with a quartz crystal microbalance with dissipation monitoring. *Macromol. Biosci.* **2008**, *8*, 410–416.
- (62) Pomorska, A.; Shchukin, D.; Hammond, R.; Cooper, M. A.; Grundmeier, G.; Johannsmann, D. Positive frequency shifts observed upon adsorbing micron-sized solid objects to a quartz crystal microbalance from the liquid phase. *Anal. Chem.* **2010**, *82*, 2237–2242.
- (63) Olsson, A. L.; van der Mei, H. C.; Johannsmann, D.; Busscher, H. J.; Sharma, P. K. Probing colloid–substratum contact stiffness by acoustic sensing in a liquid phase. *Anal. Chem.* **2012**, *84*, 4504–4512.
- (64) Lapidot, T.; Campbell, S.; Heng, K. L. J. Y., Model for interpreting surface crystallization using quartz crystal microbalance: theory and experiments. *Anal. Chem.* **2016**, *88*, 4886–4893.
- (65) Grunewald, C.; Schmudde, M.; Noufele, C. N.; Graf, C.; Risse, T. Ordered structures of functionalized silica nanoparticles on gold surfaces: Correlation of quartz crystal microbalance with structural characterization. *Anal. Chem.* **2015**, *87*, 10642–10649.
- (66) Olsson, A. L.; Quevedo, I. R.; He, D.; Basnet, M.; Tufenkji, N. Using the quartz crystal microbalance with dissipation monitoring to evaluate the size of nanoparticles deposited on surfaces. *ACS Nano* **2013**, *7*, 7833–7843.